Modulating perovskite crystallization process towards highly efficient and stable perovskite solar cells via MXene quantum dots modified SnO_2

Yingguo Yang[1,2,#,*], Haizhou Lu[3,4,#], Shanglei Feng[1,2,#], Lifeng Yang[1,2,#], Hua Dong[5], Jiaou Wang[6], Chen Tian[1,2], Lina Li[1,2], Hongliang Lu[7], Jaeki Jeong[3], Shaik M. Zakeeruddin[4], Yuhang Liu[4,*], Michael Grätzel[4,*], Anders Hagfeldt[3,8,*]

[1]Shanghai Synchrotron Radiation Facility (SSRF), Zhangjiang Lab, Shanghai Advanced Research Institute, Shanghai Institute of Applied Physics, Chinese Academy of Sciences, Shanghai 201204, China.
[2]University of Chinese Academy of Sciences, Beijing 100049, China
[3]Laboratory of Photomolecular Science, Institute of Chemical Sciences Engineering, École Polytechnique Fédérale de Lausanne (EPFL), CH-1015 Lausanne, Switzerland.
[4]Laboratory of Photonics and Interfaces, Institute of Chemical Sciences and Engineering, EPFL, CH-1015 Lausanne, Switzerland.
[5]Key Laboratory for Physical Electronics and Devices of the Ministry of Education & Shaanxi, Xi'an Jiaotong University, China.
[6]Institute of High Energy Physics, Chinese Academy of Sciences, Beijing 100049, China.
[7]School of Microelectronics, Fudan University, Shanghai 200433, China.
[8]Current address: Department of Chemistry, Ångström Laboratory, Uppsala University, Box 523, 751 20 Uppsala, Sweden.

[#]These authors contributed equally to this work.

[*]Corresponding author. Email: yangyingguo@sinap.ac.cn (Y.Y.); yuhang.liu@epfl.ch (Y.L.); michael.graetzel@epfl.ch (M.G.); anders.hagfeldt@uu.se (A.H.).

Abstract: Nanocrystalline tin (IV) oxide (SnO_2) electron-transport layers (ETL) have shown great potential for achieving highly efficient, stable perovskite solar cells (PSCs), especially for the low-temperature processed flexible PSCs. Recently, studies have further shown that a modified SnO_2 bottom layer facilitates the deposition of highly crystalline perovskite films, boosting the photovoltaic performance of the PSCs. Modulating perovskite crystallization process is a key to obtain highly crystalline and stable perovskite film, however, a fundamental understanding is still missing. Herein, we report an *in-situ* synchrotron-based two-dimensional grazing incidence X-ray diffraction technique to explore the SnO_2 ETL modulated perovskite crystallization kinetics for the first time. The titanium carbide (Ti_3C_2)-MXene quantum dots are used to modify SnO_2 ETL, which is found to be able to rapidly induce perovskite nucleation from the precursor solution, forming an intermediate perovskite phase upon anti-solvent

treatment. This substantially improves the crystal quality and phase stability of the as-fabricated perovskite film. Benefiting in addition from the superior charge extraction properties of the MQDs modified SnO_2 layer, a steady-state power conversion efficiency of up to 23.3%, as well as outstanding stability against humidity and light soaking were achieved for the corresponding PSCs.

Keywords: MXene quantum dots doped SnO_2; crystallization kinetics; *in-situ* GIXRD; efficient and stable PSCs

Introduction

Perovskite solar cells (PSCs) have been emerged as a cutting-edge photovoltaic technique with power conversion efficiency (PCE) exceeding 25% and operational stability over thousands of hours, endowing them great potential for commercialization (*1-4*). Most of the reported high-efficiency PSCs are based on a mesoporous TiO_2 layer, however, the high sintering temperature (> 450 °C) for mesoporous TiO_2 limits the potential applications for large-area and flexible solar cell devices (*5*). In contrast, low-temperature processed nanocrystalline SnO_2 has been demonstrated as an excellent electron extraction layer, attracting intense research interests. Remarkable efforts in terms of the device architecture, perovskite precursor composition and selective extraction layers have been devoted to improving the photovoltaic performance of the SnO_2 based PSCs (*5-16*).

Low temperature processed SnO_2 electron transporting layer (ETL) has been widely investigated in the n-i-p PSCs because of its high electron mobility as well as suitable band alignment with the perovskite photo-absorber (*6-8*). Hagfeldt *et al.* demonstrated for the first time the highly efficient and hysteresis-free SnO_2-based PSCs (*6*). You *et al.* further reported a PCE of ~20% for the SnO_2-based PSCs using a sequential deposition method (*7*) and a certified PCE of 23.3% recently using a surface passivation technique (*8*). Meanwhile, it has been demonstrated that modifications of the SnO_2 bottom interlayer could significantly boost the performance of the resulting PSCs. For instance, we reported a red-carbon quantum dots modified SnO_2 (RCQs-SnO_2) ETL with a high electron mobility of 1.73×10^{-2} cm^2/Vs, which was successfully used to boost the PCE of the corresponding PSCs up to 22.77% (*12*). Similarly,

metal-doped SnO_2 ETL has been demonstrated to be able to improve the device performance due to the improved charge carrier mobility (*15*).

We noticed that the perovskite films deposited on RCQs-SnO_2 ETL had a more uniform morphology as well as better crystallinity and stability compared to perovskite films deposited on pristine SnO_2 ETL. In addition, potassium (*17*), chloride (*18*) or organic ligand modified bottom interlayer (*19*) could also induce an improved crystallinity of the top perovskite layer. We know that a good crystallinity and a low defect density of the perovskite films are key factors to achieve high-performance PSCs. Thus, it is of vital importance to understand the fundamentals of the SnO_2 ETL modulated crystallization kinetics during the perovskite deposition process. However, to the best of our knowledge, the exploration of the relationship between SnO_2 surface functionalization and relevant crystallization kinetics of the top perovskite layer are rarely reported.

Recently, a class of two-dimensional (2D) transition metal carbides and nitrides, MXenes, have been studied for the application of PSCs (*20-21*) owning to their unique optoelectronic properties and tunable surface properties. Agresti *et al.* (*20*) reported that MXenes with various termination groups could be used to tune the work function of the perovskite layer and TiO_2 ETL. Yang *et al.* (*21*) reported that the electron mobility and charge extraction of SnO_2 could be improved by mixing it with MXene ($Ti_3C_2T_x$), leading to an increased PCE of the corresponding PSCs. Inspired by the promising features of MXenes, we synthesized N, S, co-doped $Ti_3C_2T_x$ quantum dots (MQDs) aiming to engineer the perovskite/SnO_2 ETL interface.

To reveal the rationale of MQDs modified SnO_2 (MQDs-SnO_2) ETL induced crystallization kinetics of the top perovskite layer, we performed *in-situ* synchrotron-based two-dimensional grazing incidence X-ray diffraction (2D-GIXRD) study on crystallization kinetics of the perovskite film. Unlike the crystallization process on the SnO_2 ETL without MQDs, we found an obviously modulated crystallization procedure of the perovskite layer deposited on MQDs-SnO_2 ETL. A largely increased nucleation rate of perovskite crystals during the initial spin-coating process was observed for perovskites on MQDs-SnO_2 substrate and an intermediate perovskite phase was formed after anti-solvent treatment, yielding high-quality perovskite

crystals with preferred orientation during the annealing process, leading to improved photovoltaic performance and stability of the corresponding PSCs.

Results and discussions

Figure S1 shows the transmission electron microscopy (TEM) images of the pristine SnO_2 (Fig. S1(a)) and MQDs-SnO_2 (Fig. S1(b)) nanocrystal films, which are deposited on copper mesh and baked treatment respectively. Both SnO_2 and MQDs nanoparticles were well dispersed and no obvious aggregations can be observed. Figure S2 shows the energy dispersive X-ray (EDX) mapping of MQDs-SnO_2 nanocrystals film, which demonstrates a uniform distribution of MQDs in SnO_2 matrix. Figure S3 shows the scanning electron microscopy (SEM) and atomic force microscopy (AFM) images of the spin-coated SnO_2 and MQDs-SnO_2 films. The MQDs-SnO_2 film had a smoother and more uniform surface morphology than the reference SnO_2 film. Figure S4(a) shows a calculated electron mobility of ~8.0×10^{-3} cm^2 V^{-1} s^{-1} for the MQDs-SnO_2 film, which is significantly higher than that of the pristine SnO_2 (~9.0×10^{-4} cm^2 V^{-1} s^{-1}). Figure S4(b) demonstrates higher conductivity of MQDs-SnO_2 than the pristine SnO_2. Figure S5 shows the GIXRD patterns of the SnO_2 films with and without MQDs. The dominate lattice plane of the pristine SnO_2 film is (110), whereas the dominate lattice planes of the MQDs-SnO_2 film are (110), (101) and (211), which demonstrates the un-stabilized and high-active crystal planes emerged in the MQDs-SnO_2 due to the modification of MQDs. Figure S6 shows identical optical absorptions for both pristine SnO_2 and MQDs-SnO_2 films. X-ray photoelectron spectroscopy (XPS) was also performed to investigate the interactions between SnO_2 and MQDs. Figure S7 shows the Sn $3d_{3/2}$ peaks at ~486.50 and ~495.05 eV for the pristine SnO_2 film. The fact that the corresponding peaks shifted to lower positions at ~485.99 and ~494.41 eV for the MQDs-SnO_2 film indicates an increased electron density around Sn atoms. Ultraviolet photoelectron spectroscopy (UPS) was performed to investigate the electronic structure of the SnO_2 ETLs. Figure S8 shows an up-shift of the MQDs-SnO_2 ETL Fermi level from -4.39 eV for the control SnO_2 ETL to -4.12 eV for MQDs-SnO_2 ETL, indicating a better energy level matching between the MQDs-SnO_2 ETL and perovskite film (~ -4.15 eV) (*22*), facilitating the electron extraction from the perovskite to SnO_2 ETL (*12, 18*).

We fabricated the perovskite films with a composition of $FA_{0.9}MA_{0.05}Cs_{0.05}PbI_{0.98}Br_{0.02}$ on top of the SnO_2 nanocrystalline ETLs using a one-step spin-coating method with antisolvent treatment. Details of the perovskite precursor preparation and deposition method can be found in the supplementary materials (SM). Figure 1, A and B show the top-view SEM images of both SnO_2-based perovskite (reference) and MQDs-SnO_2-based perovskite (target) films. Both present compact perovskite layers, while the target perovskite film showed more uniform and larger grain sizes than the reference. Figure S9 shows an averaged grain size of ~850 nm for MQDs-SnO_2 modulated perovskite film which is significantly larger than that (~500 nm) of the reference sample. Figure 1C shows the Ultraviolet-visible (UV-*Vis*) absorption and photoluminescence (PL) spectra of the reference and target films. The target film showed an enhanced absorption in the visible region than the reference film, which is supposed to be related to the improved crystallinity of the perovskite film on MQDs-SnO_2, which is discussed in the following text. Time-resolved photoluminescence (TRPL) is applied to monitor the charge extraction behavior of MQD-SnO_2, shown in Fig. 1D. The fitted lifetime of the MQD-SnO_2 film (55.2 ns) is much shorter than that (100.5 ns) of the pristine film, which indicates a better charge extraction of the bottom MQDs-SnO_2 ETL than the pristine SnO_2 ETL. 2D-GIXRD patterns of both the reference and target perovskite films (Fig. 1, E and F) shows similar diffraction rings and spotty patterns. Compared with the reference perovskite film, the target one shows much brighter scattered rings at $q \approx 10$, 20 and 22.2 nm^{-1}, which indicates a better crystallinity and better out-of-plane orientations.

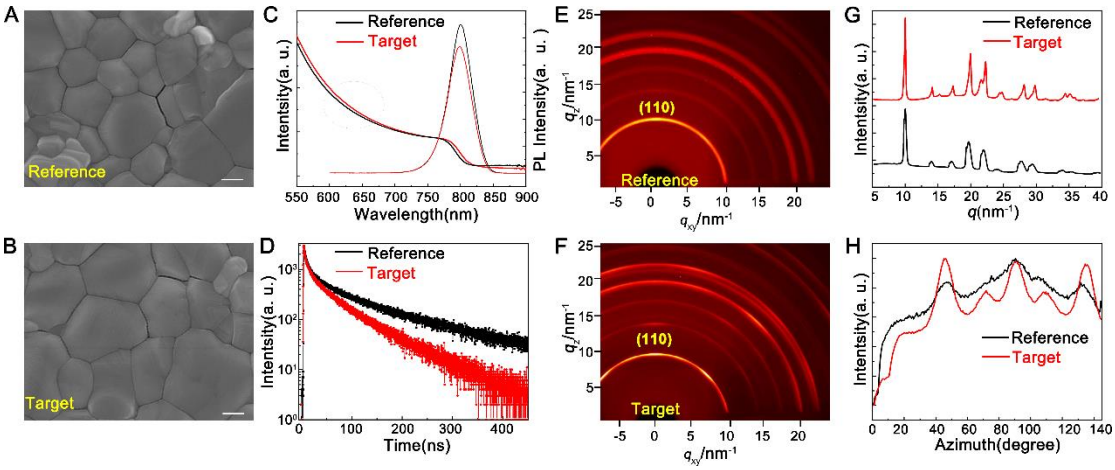

Figure 1. **Characterization of the perovskite films.** SEM images of the reference (**A**) and target (**B**)

perovskite films, scale bar is 200 nm; (**C**) UV-Vis absorption and PL spectra of the reference and target perovskite films; (**D**) The TRPL spectra of the reference and target perovskite films; 2D-GIXRD patterns of the reference (**E**) and target (**F**) perovskite films; (**G**) Integrated 1D GIXRD spectra of the reference and target perovskite films; (**H**) Radially integrated intensity plot for the (110) diffraction peaks of the reference and target perovskite films.

The azimuthally integrated 1D GIXRD spectra (Fig. 1G) derived from the 2D-GIXRD patterns (Fig. 1, E and F) further showed that the target film had higher and sharper (110) diffraction peaks than the reference film. The narrow full width at half maximum (FWHM) of the diffraction peaks of the target film could be associated with its relatively large perovskite crystalline size, consistent with the SEM images shown in Fig. 1, A and B (*12*, *23-25*). Figure 1H presents the radially integrated intensity plots along the (110) diffraction ring ($q \approx 10$ nm^{-1}) plotted as a function of azimuth angle φ for both the reference and target perovskite films. The (110) planes of both films exhibited a multi-order preferential orientation at azimuth angles of 45°, 67.5° and 90°. The target perovskite film had a narrower FWHM for any above azimuth angle comparing with the reference film, indicating a much more ordered structure with a preferential crystal orientation (*25*). The azimuthally integrated 1D GIXRD prove that MQDs-SnO_2 favors a multi-ordered preferential (110) orientation and crystallization of the deposited top perovskite layer (*12, 24, 25*).

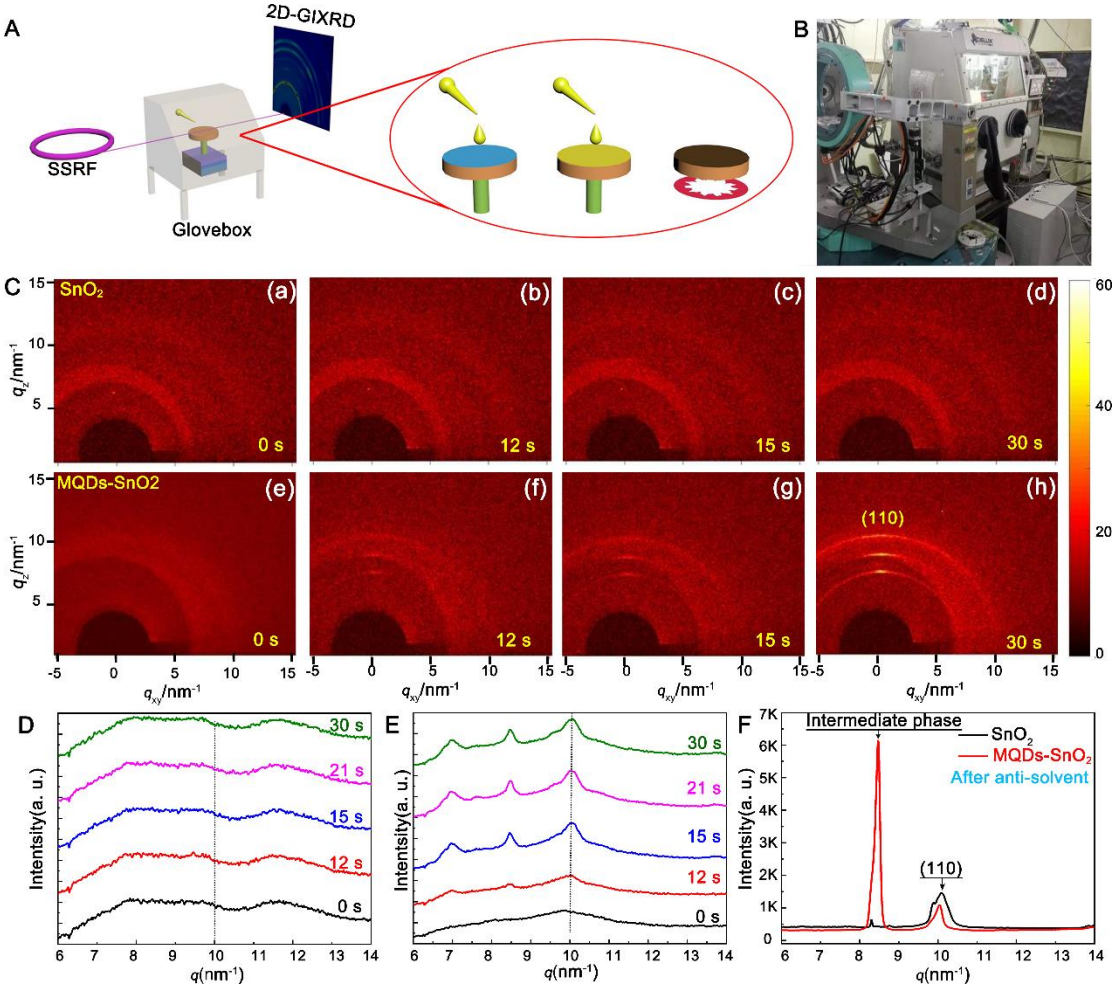

Figure 2. **GIXRD measurements during the perovskite fabrication process on both SnO_2 and MQDs-SnO_2 ETLs.** (**A**) A schematic for *in-situ* GIXRD measurements during the perovskite spin-coating process; (**B**) A picture of the *in-situ* GIXRD experimental setup including a customized mini glove box (volume content (H_2O, O_2) <1 ppm); (**C**) The 2D-GIXRD patterns of the deposited perovskite films as a function of the spin-coating time; The integrated 1D-GIXRD spectra of perovskite films deposited on pristine SnO_2 (**D**) and MQDs-SnO_2 (**E**) ETLs before the antisolvent treatment; (**F**) The integrated 1D-XRD spectra of the perovskite films after antisolvent treatment.

To explore the MQD-SnO_2 ETL induced crystallization kinetics of the perovskite film, *in-situ* 2D-GIXRD measurements were performed from the spin-coating of perovskite precursor solution on both pristine SnO_2 and MQDs-SnO_2 ETLs until calcination of the perovskite. Figure 2A shows a schematic of the *in-situ* GIXRD measurements during the spin-coating process of the perovskite film. Figure 2B is a photo of the experimental setup used for this study. After dropping the perovskite precursor solution onto the SnO_2 substrates, the 2D-GIXRD patterns

were recorded every 0.5 s during the spin-coating process for 30 s. To simulate the real device fabrication condition, the whole spin-coating processes were performed in a customized mini glove box with controlled amount of water and oxygen levels (H_2O and O_2 < 1 ppm). Figure 2C shows the 2D-GIXRD patterns of the perovskite films deposited on pristine SnO_2 (a-d) and MQDs-SnO_2 (e-h) ETLs as a function of the spin-coating time. Different from the perovskite film deposited on pristine SnO_2, the perovskite film deposited on MQDs-SnO_2 ETL showed bright diffraction rings and spots starting from 12 s, which indicated a rapid nucleation process during the spin-coating stage before anti-solvent treatment. Supplementary movies S1 and S2 display the evolution of 2D-GIXRD patterns during the whole spin-coating process.

Figure 2D and 2E show the azimuthally integrated intensity plots derived from the 2D-GIXRD patterns of the perovskites fabricated on pristine SnO_2 and MQDs-SnO_2 ETLs, respectively. For the perovskite film grown on pristine SnO_2 (Figure 2D), there was no obvious peaks of perovskite phase but several broad bumps, indicating the amorphous nature of the perovskite precursor without any sign of conversion into perovskite crystals before the antisolvent treatment. This is also consistent with the previous report by Dounya Barrit *et al.* that a disordered colloidal state without a diffraction signature was observed for the initial spin-coating process *(26)*. Differently, for the perovskite films grown on the MQD-SnO_2 ETL, a few peaks could be clearly observed at ~12 s of the spin-coating process. The peaks at $q \approx 7$ nm^{-1} and $q \approx 8.5$ nm^{-1} are assigned to perovskite intermediate phases *(12, 24, 25, 27)*, and the diffraction peak at $q \approx 10$ nm^{-1} is known to be the tetragonal perovskite (110) phase. It is noted that all these diffraction peaks increased rapidly during the 12 to 15 s time region and then remained almost constant until 30 s, giving an appropriate time window for the subsequent antisolvent treatment. Similar but weaker diffraction patterns were also observed for the perovskite film deposited on our previously reported RCQs-SnO_2 ETL, as shown in Figure S10 (*12*).

After the anti-solvent treatment, the integrated 1D-GIXRD spectra of the reference and target perovskite films were presented in Figure 2F. The small diffraction peaks at $q \approx 10$ nm^{-1} for both films indicate a small amount of perovskite crystals formed right after the antisolvent treatment. Different from the control film, the target film had a new diffraction peak at $q \approx 8.5$

nm^{-1}, which is the dominating intermediate perovskite phase during the whole spin-coating period. It is well known to the PSC field that an intermediate phase is crucial for the final crystallization of the perovskite *(27, 28)*. Our results are consistent with the previous reports that quantum-dot materials including graphene oxides and RCQs could increase the nucleation rate of crystalline perovskite as well as the intermediate perovskite phase (*11-14*).

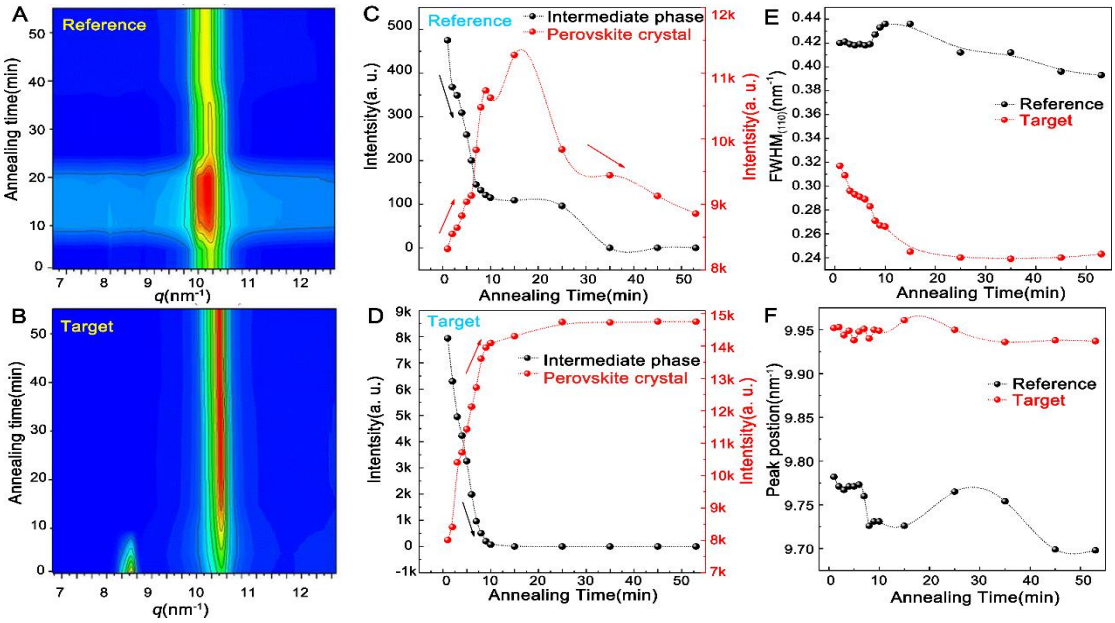

Figure 3. **GIXRD measurements of the perovskite films during the annealing process.** The integrated 1D-GIXRD spectra of reference (**A**) and target (**B**) perovskite films at different annealing time; Diffraction intensity (peak area) of the reference (**C**) and target (**D**) perovskite films at different annealing time; FWHM (**E**) and peak position (**F**) of perovskite (110) diffraction peak of both reference and target perovskite films plotted as functions of annealing time.

We continued the *in-situ* real-time 2D-GIXRD measurements during the subsequent annealing process to investigate the transformation from intermediate phase to the final perovskite phase. The annealing process was carefully monitored, starting gradually from room temperature to 100 °C within the initial 2 minutes (stage I) and remained at 100 °C for the following 10 minutes (stage II), then to 150 °C for 35 minutes (stage III). Figure S11 shows the 2D-GIXRD patterns of the perovskite films annealed at five different time points. Figure 3A and 3B show the azimuthally integrated intensity profiles derived from these 2D-GIXRD patterns, demonstrating a gradual structural evolution from distinct intermediate perovskite crystals into

highly ordered perovskite crystals during the annealing process.

Figure 3C shows the change of the perovskite peak intensity of the reference film with annealing time. For the perovskite intermediate phase ($q \approx 8.5$ nm^{-1}), it gradually decreased with increasing annealing time and disappeared at 25 minutes, whereas the perovskite (110) phase ($q \approx 10$ nm^{-1}) increased till ~20 min, then decreased gradually in the last 10 mins, indicating a poor thermal stability for the reference perovskite film. Figure 3D shows the change of the perovskite peak intensity of the target film with annealing time. It showed a rapid conversion from intermediate perovskite phase to highly crystalline perovskite phase within 10 minutes at 100 ℃ and the perovskite phase remained almost constant at 150 ℃ for 15 mins, indicating an improved thermal stability for the target perovskite film as compared to the reference.

Figure 3E shows the FWHM of the perovskite (110) peaks of both the reference and target perovskite films. The FWHM of the target film was larger than that of the reference film during the whole annealing process, indicating bigger average size domains formation. For the target perovskite film, the FWHM of perovskite (110) peak gradually decreased with increasing the annealing time up to 20 minutes and then kept almost constant. Figure 3F shows the perovskite (110) peak positions of both reference and target perovskite films as a function of the annealing time. The fluctuation of perovskite (110) diffraction peak of the target film during the annealing was relatively smaller compared to that of the control film. All these results indicated that the target film had a better crystallinity and thermal stability at up to 150 °C compared to the reference film.

Real time *in-situ* GIXRD measurements were also performed for the films heated at 100 ℃ in an ambient environment with 40-60% relative humidity, and the results are shown in Figure S12 ((a)-(c)). The perovskite diffraction peak of the reference film decreased much faster than that of the target one, suggesting that the MQDs-SnO_2 ETL is crucial for achieving the thermal and moisture resistant perovskite films. SEM images of the perovskite films heated at 100 ℃ in an ambient environment with 40-60% relative humidity are shown in Figure S12 ((d)-(e)). The reference film presented more bright islands whereas the target film remained smooth and

lager grains. Figure S13 shows the cross-sectional SEM images of perovskite/ETL interfaces. Compared with the interface between perovskite and pristine SnO_2 ETL, the morphology of perovskite/MQDs-SnO_2 ETL interface is shown to be smoother without obvious pinholes, indicating a larger textured domains and inter-connected grain boundaries within the perovskite film grown on MQDs-SnO_2 ETL. Figure S14 shows the cross-sectional high-resolution TEM (HR-TEM) images of the perovskite/SnO_2 ETL/ITO interface and the perovskite/MQDs-SnO_2 ETL/ITO interface, respectively. Compared with the distribution of SnO2 ETL showed Figure S14(a), the lattice distribution of MQDs presented uniformly in the complex SnO2 matrix as shown in Figure S14(b). Notably, the interface of perovskite/MQDs-SnO_2 ETL illustrates much more lattice fringes in perovskite layer compared with that of perovskite/SnO_2 ETL, which indicates a higher crystalline of perovskite film grown on MQDs-SnO_2 ETL. Figure S15 and Figure S16 show a well-matched band alignment between perovskite film and SnO_2 ETL after MQDs modification, which would effectively promote electron extraction in the PSCs with reduced charge accumulation at the ETL/perovskite interface.

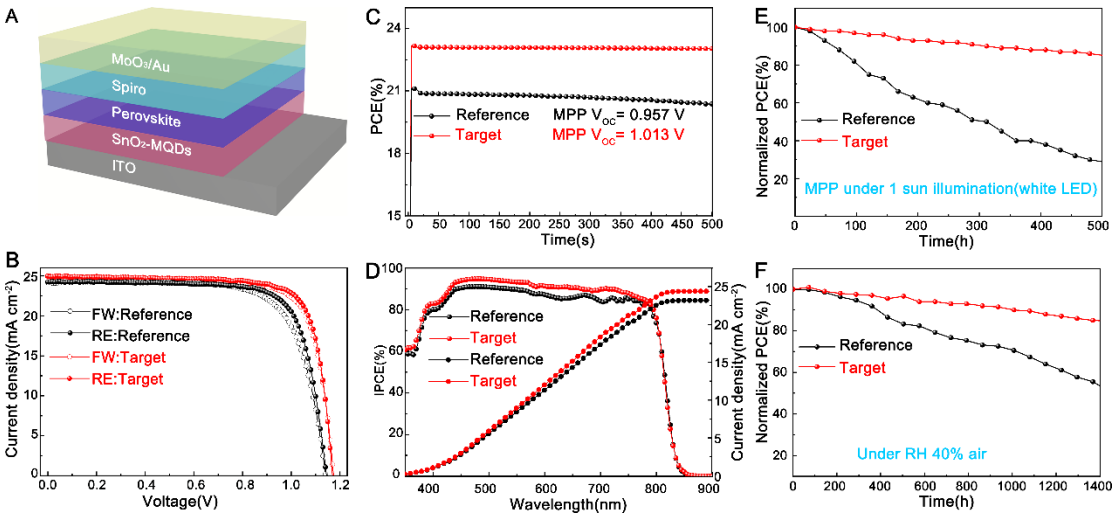

Figure 4. PV performance of the PSCs. (**A**) Schematic of the planar heterojunction structure used for the SnO_2-based PSCs; (**B**) The *J*-V curves of one of the best SnO_2-based and MQDs-SnO_2-based PSCs devices under both forward and reverse scans; (**C**) The stabilized steady state power output of the reference and target PSCs at the maximum power output point at 0.957 and 1.013 V bias respectively; (**D**) The IPCE curves and integrated current density of these two devices. (**E**) Long-term light-exposition stability of the reference and target PSCs without

encapsulation; (**F**) The PCE of reference and target PSCs without encapsulation as a function of exposure time in an ambient environment with 40% RH at 25 ℃.

We then fabricated PSC devices using an ITO/SnO_2/Perovskite/Spiro-MeOTAD/MoO_3/Au (ITO, indium tin oxide; Spiro-MeOTAD, 2,2′,7,7′-tetrakis[*N*,*N*-bis(*p*-methoxyphenyl)amino]-9,9′-spirobifluorene; MoO_3, molybdenum oxide) configuration as illustrated in Fig. 4A. Figure 4B shows a PCE of 20.96% with a short-circuit current density (J_{sc}) of 24.26 mA cm^{-2}, a V_{oc} of 1.140 V, and a fill factor (FF) of 0.758 for the reference device. The champion target device achieved a maximum PCE of 23.34 % with a J_{sc} of 24.96 mA cm^{-2}, a V_{oc} of 1.172 V, and a FF of 0.798. The detailed *J*-V parameters for the optimization of MQDs-SnO_2 are summarized in the SM (Figs. S17, S18 and Tables S1, S2). We note that no obvious hysteresis could be found for the target device between forward and reverse scan, which could be related to the superior electron extraction and transport properties of MQDs-SnO_2 (*29-32*). Figure 4C shows the stabilized PCE at a constant voltage bias of 0.957 V and 1.013 V, which is the voltage under maximum power point (MPP) output of the reference and target PSCs, respectively. Compared with the control device, the steady power output of the target cell reached up to ~23% and stabilized for 500 s at a bias voltage of 1.013 V, confirming the enhanced PCE of PSCs induced by MQDs modification. Figure 4D shows the incident photon-to-electron conversion efficiency (IPCE) and the integrated current density (J_{sc}) for both the reference and target PSCs. Compared with the reference device, the target device had a higher IPCE over the entire visible light region with the integrated J_{sc} up to ~24.39 mA cm^{-2}, which agrees well with the measured J_{sc} ~ 24.96 mA cm^{-2} under solar simulator. Table S3 shows the photovoltaic parameters of the best PSCs fabricated on bare SnO_2, RCQs-SnO_2, MQDs-SnO_2 ETLs. Clearly, the MQDs-SnO_2-based device showed the best performance demonstrating the advantage of treating the colloidal SnO_2 particles with MQDs modulation.

Figure 4E shows the light soaking stability of the PSC devices under simulated one-sun illumination, which prove that the target PSCs are much more resistant to light stress than the control device without MQDs. There are less than 10% efficiency losses after 500 h continuous simulated one-sun illumination for target PSCs, whereas the measured PCEs presented over 20% losses for the control PSCs under the same conditions. Figure 4F shows the shelf stability of

the un-encapsulated PSC devices stored in an ambient environment with 40-60% RH at 25 ℃. The PCE of the target cell remained ~90% of its initial value after 500-hour storage, whereas the reference PSC decreased down to ~80% of its initial value. Figure S19 shows the thermal stability test of the control and target PSCs by annealing them at 60 ℃ for 120 hours. The normalized PCEs of both devices without encapsulation are plotted as a function of the exposure time in an ambient environment with ~25% relative humidity at 60°C. Notably, the PCE of the MQDs-SnO_2-based PSC dropped much less compared with the reference cell, demonstrating that the novel MQDs-SnO_2 ETL enhances the thermal stability of planar PSCs significantly over those based on a pristine SnO_2 ETL. These stability test indicated that perovskite films grown on the MQDs-SnO_2 ETL were more robust against the erosion of light, moisture, heat, and oxygen.

Conclusion

In summary, we report here highly efficient and stable PSCs employing a MQDs modified nanocrystalline SnO_2 ETL. Synchrotron based *in-situ* 2D-GIXRD measurements were performed during the perovskite deposition process to investigate the bottom SnO_2 ETL induced crystallization kinetics of the perovskite film. It was found that the MQDs-SnO_2 ETL modulated crystallization was crucial for the performance and stability of the resulting PSCs. The in-depth study of the crystallization process from the nucleation and intermediate phase, to the calcinated perovskite phase provide an effective approach for fabricating high-quality perovskite films on a planar ETL. Our work provides a general methodology for understanding the perovskite crystallization, which is considered as one of the most important research topics in the perovskite community.

References

(1) https://www.nrel.gov/pv/cell-efficiency.html(2020)

(2) Zonghao Liu, *et al*. A holistic approach to interface stabilization for efficient perovskite solar modules with over 2,000-hour operational stability. *Nat. Energy*, **5**, 1 - 9 (2020)

(3) Yen-Hung Lin, *et al*. A piperidinium salt stabilizes efficient metal-halide perovskite solar cells. *Science* **369**, 96–102 (2020)

(4) Xiaopeng Zheng, *et al*. Managing grains and interfaces via ligand anchoring enables 22.3%-efficiency inverted perovskite solar cells. *Nat. Energy*, **5**, 131–140(2020).

(5) Juan Pablo Correa Baena, *et al*. Highly efficient planar perovskite solar cells through band alignment engineering. *Energy Environ. Sci.,* **8***,* 2928-2934 (2015).

(6) Haizhou Lu, *et al*. Vapor-assisted deposition of highly efficient, stable black-phase $FAPbI_3$ perovskite solar cells. *Science,* **370**, eabb8985 (2020).

(7) Qi Jiang, *et al*. Planar-structure perovskite solar cells with efficiency beyond 21%. *Adv. Mater.*, **29**, 1703852 (2017).

(8) Qi Jiang, *et al*. Surface passivation of perovskite film for efficient solar cells. *Nat. Photonics,* **13**, 460–466 (2019).

(9) Ajay Kumar Jena, *et al*. Halide perovskite photovoltaics: background, status, and future prospects. *Chemical Reviews* **119**, 3036-3103 (2019).

(10) Eui Hyuk Jung, *et al*. Efficient, stable and scalable perovskite solar cells using poly(3-hexylthiophene). *Nature*, **567**, 511–515 (2019).

(11) Meng Li, *et al*. Graphdiyne-modified cross-linkable fullerene as an efficient electron transporting layer in organometal halide perovskite solar cells, *Nano Energy*, **43**, 47–54 (2018).

(12) Wei Hui, *et al*. Red-carbon quantum dots doped SnO_2 composite with enhanced electron mobility for efficient and stable perovskite solar cells. *Adv. Mater.,* 3**2**, 1906374 (2020).

(13) Meng Li, *et al.* Perovskite grains embraced in a soft fullerene network make highly efficient flexible solar cells with superior mechanical stability. *Adv. Mater.*, **32**, 1901519 (2019).

(14) Zhaokui Wang, *et al.* Induced perovskite crystallization by perylene for high-performance solar cells. *ACS Nano* **10**, 5479-5489 (2016).

(15) Qi Liu, *et al.* Effect of tantalum doping on SnO_2 electron transport layer via low temperature process for perovskite solar cells. *Appl. Phys. Lett.* **115**, 143903 (2019).

(16) Tiefeng Liu, *et al*. Tailoring vertical phase distribution of quasi-two-dimensional perovskite films via surface modification of hole-transporting layer. *Nat. Commun.*, **10**, 878 (2019).

(17) Singh Trilok, *et al*. Sulfate-assisted interfacial engineering for high yield and efficiency of triple cation perovskite solar cells with alkali-doped TiO_2 electron-transporting layers. *Adv. Funct. Mater.* **28**, 1706287 (2018).

(18) Hairen Tan, *et al.* Efficient and stable solution-processed planar perovskite solar cells via contact passivation. *Science*, **355**, 722-726 (2017).

(19) Shengfan Wu, *et al.* Modulation of Defects and Interfaces through Alkylammonium interlayer for efficient inverted perovskite solar cells. *Joule*, **4**, 1–15 (2020).

(20) Antonio Agresti, *et al*. Titanium-carbide MXenes for work function and interface engineering in perovskite solar cells. *Nat. Mater.*, **18**, 1228 (2019).

(21) Lin Yang, *et al*. Surface-modified metallic $Ti_3C_2T_x$ MXene as electron transport layer for planar heterojunction perovskite solar cells. *Adv. Funct. Mater.*, **29**, 1905694 (2019).

(22) Nengxu Li, *et al*. Energy level modulation in diboron modified SnO_2 for high efficiency perovskite solar cells. *Solar RRL,* **4***,* 1900217(2019)

(23) Minchao Qin, *et al.* Manipulating the mixed-perovskite crystallization pathway unveiled by in situ GIXRD. *Adv. Mater.,* **31**, 1901284 (2019).

(24) Yingguo Yang, *et al.* Annealing induced re-crystallization in $CH_3NH_3PbI_{3-x}Cl_x$ for high performance perovskite solar cells. *Scientific Reports*, **7**, 46724 (2017).

(25) Yingguo Yang, *et al.* Interfacial engineering and film-forming mechanism of perovskite films revealed by synchrotron-based GIXRD at the SSRF for high-performance solar cells. *Materials Today Advances,* **6**, 100068 (2020).

(26) Dounya Barrit, *et al.* Room-Temperature Partial Conversion of α-$FAPbI_3$ Perovskite Phase via PbI_2 Solvation Enables High-Performance Solar Cells. *Adv. Funct. Mater.*, **30**, 1907442 (2019).

(27) Kai Zhang, *et al.* A prenucleation strategy for ambient fabrication of perovskite solar cells with high device performance uniformity. *Nat. Commun.*, **11**, 1006(2020).

(28) Nam Joong Jeon, *et al.* Solvent engineering for high-performance inorganic-organic hybrid perovskite solar cells. *Nat. Mater.*, **13**, 897-903 (2014).

(29) Yongzhen Wu, *et al.* Perovskite solar cells with 18.21% efficiency and area over 1cm^2 fabricated by heterojunction engineering, *Nat. Energy*, **1**, 16148 (2016).

(30) Jingjing Zhao, *et al*. Strained hybrid perovskite thin films and their impact on the intrinsic stability of perovskite solar cells. *Science Advances* **3**, eaao5616 (2017).

(31) Chunsheng Jiang*, et al.* Carrier separation and transport in perovskite solar cells studied by nanometer-scale profiling of electrical potential. *Nat. Commun.*, **6**, 8397 (2015).

(32) Mojtaba Abdi-Jalebi, *et al.* Charge extraction via graded doping of hole transport layers gives highly luminescent and stable metal halide perovskite devices. *Science Advances* **5**, eaav2012 (2019).

Acknowledgements

We acknowledge Renduo Liu from SINAP and Shilong Lv from SIMIT for assisting with HR-TEM sample preparation and measurement. This work is supported by the National Key Research and Development Program of China (2017YFA0403400), the National Natural Science Foundation of China (Grant Nos. 12075309, 11605278, 11705271, U1632121), and the research grant (No.17YF1423700) from the Shanghai Sailing Program, Shanghai Municipal Commission for Science and Technology (No. 20ZR1464100) and Young Innovator Association of CAS. The authors thank beamline BL17B1, BL11B, BL14B1, BL16B1, BL19U, BL08U and BL01B1 staff at the SSRF for providing the beamtime and valuable discussions. A.H. thanks the Swiss National Science Foundation for support (project "Fundamental studies of dye-sensitized and perovskite solar cells" funded by grant no. 200020_185041). M.G. acknowledges financial support from the European Union's Horizon 2020 research and innovation grant (grant no. 826013) and the King Abdulaziz City for Science and Technology

(KACST).

Competing interests: The authors declare no competing interests.

Author contributions: Y.Y. and S.F. recorded and analyzed the SEM images, UV-visible absorption, PL, TRPL and GIXRD spectra. Y.Y., L.Y and H.D. fabricated the devices and characterized their performance. J.W. performed XPS and UPS measurements. C.T and L.L helped the SEM cross section, SCLC and AFM measurement. H.L. J.J and S.M.Z coordinated the work. Y.Y., H.L. and Y.L. analyzed the data and drafted the manuscript. A.H. and M.G. suggested some experiments and revised the manuscript. H.L. and A.H. replied to the referees' comments. All authors contributed to the discussion.